

# Effect of deformation processes in austenite region on microstructure and mechanical properties in a Si-Mn hot-rolled TRIP steel

YingJie Yu, Hua Qin, BingXin Wang\*

*College of Mechanical Engineering, Liaoning Petrochemical University, Fushun 113001, P. R. China*

Received 21 October 2024, received in revised form 27 December 2024, accepted 27 January 2025

## Abstract

A Si-Mn hot-rolled TRIP steel was subjected to different deformation in austenite recrystallization and non-recrystallization regions during thermo-mechanical processes. The microstructural characteristics were analyzed using optical microscopy, transmission electron microscopy (TEM), X-ray diffraction (XRD) and electron back-scattered diffraction (EBSD), and its effects on mechanical properties were investigated. The results show that a bigger reduction in deformation in the austenite non-recrystallization region results in a more remarkable pancaking of the austenite grain. This austenite condition strongly promotes proeutectoid ferrite formation, which causes an increase in the amount of retained austenite (RA). Compared with the case of smaller reduction in austenite non-recrystallization region, the steel with bigger reduction exhibits higher elongation and excellent combination of strength and ductility because of higher fractions of proeutectoid ferrite and RA particles with different sizes that provide sustained transformation-induced plasticity (TRIP) effect over a significantly wide strain range. The untransformed RA in the fractured tensile specimen has a much smaller grain size and higher carbon content than the case before the fracture.

**Key words:** hot-rolled Si-Mn TRIP steel, hot rolling schedule, austenite pancaking, multi-phase microstructure, retained austenite, mechanical properties

## 1. Introduction

Hot rolled Si-Mn TRIP (transformation induced plasticity) steels possess not only the advantages of low cost of alloying elements, shorter production process and lower energy consumption but also high elongation and outstanding strength-plasticity combination [1] and are widely used to fabricate structural components with higher strength in the automobile industry. A typical Si-Mn TRIP steel microstructure is mainly comprised of polygonal ferrite along with a certain amount of bainite and small amounts of RA or martensite/austenite [2]. Under the action of external stress, the strain-induced transformation of metastable RA to martensite enhances the local strain-hardening rate, which delays the onset of necking and results in excellent elongation and combination of strength and plasticity [3–7], i.e., the TRIP effect. Accordingly, the amount and stability of RA play

a critical role in determining the mechanical properties of TRIP steels [8–12].

RA formation results from carbon partitioning between austenite and ferrite (proeutectoid and bainitic ferrite) [13, 14]. For the hot rolling process of TRIP steels, in the intercritical region of austenite + ferrite and bainite transformation temperature range, carbon is rejected from proeutectoid ferrite and bainitic ferrite to adjacent austenite during austenite to ferrite transformation. Thus, with the development of austenite decomposition transformation, the residual austenite, after the austenite transformation to ferrite, is gradually enriched with carbon accompanied by increased stability. Eventually, residual austenite obtains sufficiently high carbon content and can be stabilized at room temperature, forming RA. Therefore, the proeutectoid and bainitic ferrite formations affect the amount and stability of RA.

It is established that thermo-mechanical control

\*Corresponding author: tel.: +86 24 56863067; fax: +86 24 56865042; e-mail address: [wangbingxin@163.com](mailto:wangbingxin@163.com)

processes, particularly the rolling schedules in single-phase austenite region, are the keys to controlling austenite to ferrite transformation [15–18]. By changing deformation parameters, prior austenite state can be adjusted, and some structure changes in the austenite are introduced, such as refinement of the austenite grains due to recrystallization, occurrence of deformed bands and increase in the density of intragranular lattice defects in un-recrystallized austenite grains [19–21], which has a noticeable influence on the kinetics of subsequent transformation of austenite to ferrite. Hence, the hot-working behavior for TRIP steels is very important in adjusting prior austenite conditions to control austenite to ferrite transformation.

Conventional hot-rolled Si-Mn TRIP steel usually contains a lower Mn content of about 1.5% than medium Mn TRIP steel. The increase in Mn content decreases the stacking fault energy for austenite, which improves its work-hardening ability. Therefore, the high-temperature deformation behavior for Si-Mn TRIP steel differs from that for medium Mn TRIP steel. The literature [22] documented that conventional Si-Mn TRIP steel exhibits lower flow stress and peak strain (namely lower deformation resistance) than other types of TRIP steels with higher Mn content during high-temperature deformation. Moreover, the literature also pointed out that the steel containing higher Mn content has faster static recrystallization kinetics due to a strong work-hardening effect during deformation.

Many works have been carried out on the relationships between processes, microstructures and mechanical properties in TRIP steels. However, very few studies have investigated the prior austenite state under different high deformations, particularly its effect on RA formation courses and other microstructural constituents (polygonal ferrite and bainite). For the sake of obtaining appropriate microstructures and desirable mechanical properties by optimizing the deformation processes design, in the present work, a conventional Si-Mn TRIP steel was processed by two different deformation schedules in single-phase austenite region followed by an air cooling in the intercritical region of austenite + ferrite, and isothermal treatment in bainite transformation region. The work focuses on the morphological characteristics of prior austenite and subsequent microstructure evolution, including RA, under different deformation processes. In addition, attention is paid to strain-hardening behavior during tensile deformation (i.e., TRIP effect) and the characteristics of RA before and after the fracture of a tensile specimen.

## 2. Methods and materials

The experimental steel is a laboratory-developed

Table 1. Chemical compositions of experimental steel (mass%)

C	Si	Mn	S	P	Al
0.19	1.55	1.63	0.012	0.008	0.032

Table 2. Critical temperatures of experimental steel (°C)

$T_{nr}$	$A_{r3}$	$A_{r1}$	$B_s$
982	773	622	486

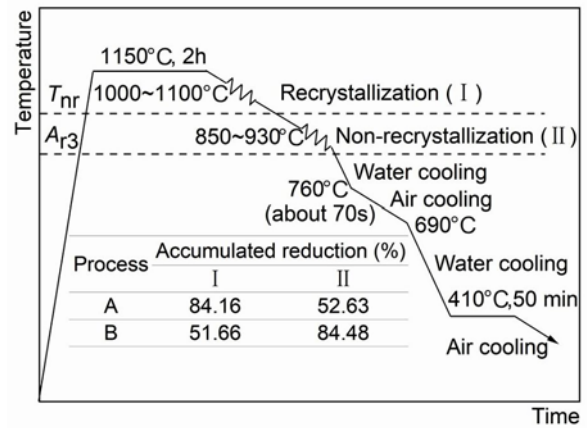


Fig. 1. Schematic diagram of thermo-mechanical control process.

low-carbon Si-Mn TRIP steel, and its chemical compositions are shown in Table 1. The experimental steel was smelted in a 150 kg vacuum induction furnace and forged into a slab billet of 60 mm in height and 100 mm in width. Several critical temperatures, including the austenite non-recrystallization temperature ( $T_{nr}$ ), were measured using the Gleeble-3500 thermomechanical simulator and listed in Table 2. Based on these temperature parameters, by varying the reduction distribution between recrystallization (Stage 1) and non-recrystallization regions (Stage 2), two reduction deformation processes of A and B in the two-stage rolling were designed, as shown in Fig. 1, and pass relative reductions were listed in Table 3. The slab billets were austenitized at 1150°C for 2 h in a resistance-heated furnace and hot-rolled into 4.5 mm thick plates in seven passes by a pilot rolling mill with twin rolls of 450 mm in diameter. After hot rolling, the steel plates were cooled to 410°C by a multi-step cooling process and held for 50 minutes in a salt-bath furnace. Moreover, to examine the austenite

Table 3. Pass reduction schedules

Stage	Pass	Process A		Process B	
		Roll gap (mm)	Relative reduction (%)	Roll gap (mm)	Relative reduction (%)
1	1	35	41.66	47	21.66
	2	18	48.57	36	23.41
	3	9.5	47.22	29	19.44
2	4	8	15.78	18	37.93
	5	6.5	18.75	11	38.88
	6	5.5	15.38	7	36.36
	7	4.5	18.18	4.5	35.71

state under different deformation conditions, after finishing rolling, two steel plates hot-rolled according to Processes A and B, respectively, were immediately quenched to room temperature rather than treated by subsequent cooling process.

The specimens for microstructure observation were machined from the steel plates, and the examined planes were parallel to the rolling direction. After mechanical polishing, the samples processed by multi-step cooling after hot rolling were etched with 4 % nital solution to reveal the metallographic microstructures. A hot-saturated aqueous picric acid solution was used for quenched specimens to display austenite morphology. All samples were observed using a Leica DMIR M Image Analyzer.

TEM analysis was conducted to investigate more detailed microstructural characteristics. The thin foils for TEM were prepared by mechanical thinning from 300 to 80  $\mu\text{m}$  along with twin-jet electropolishing in an electrolyte of 8 % perchloric acid and 92 % ethanol at the temperature of  $-30^\circ\text{C}$  and examined on an FEI Tecnai G2 F20 TEM at an accelerating voltage of 200 kV.

EBSD and XRD analyzed the characteristics of the RA phase. The specimens for EBSD and XRD were obtained using mechanical polishing followed by electrochemically polishing with 80 % ethanol, 12 % distilled water and 8 % perchloric acid (volume per cent) at a polishing voltage of 35 V. The specimens were examined at 0.02  $\mu\text{m}$  scan step on an FEI Quanta 600 SEM equipped with an EBSD system to evaluate RA particle size. The carbon content and volume fraction of RA were measured using a D/max 2400 diffractometer equipped with  $\text{CuK}_\alpha$  radiation. The specimens were scanned at a step size of  $0.04^\circ$  in the  $2\theta$  range of  $40^\circ$  to  $130^\circ$  under 55 kV and 180 mA. The integrated intensities of  $(200)_\gamma$ ,  $(220)_\gamma$ , and  $(311)_\gamma$  austenite peaks, and  $(200)_\alpha$  along with  $(211)_\alpha$  ferrite peaks were obtained by *Jade version 6.5 software* and used to calculate the volume fraction of RA ( $V_\gamma$ ) using the following equation [23, 24]:

$$V_\gamma = \frac{1.4I_\gamma}{I_\alpha + 1.4I_\gamma}, \quad (1)$$

where  $I_\gamma$  and  $I_\alpha$  are the average integrated intensities of austenite mentioned above and ferrite diffraction peaks, respectively.

The carbon concentration in the RA was estimated by the RA lattice parameter based on the  $(200)_\gamma$  peak using the following empirical expression [25]:

$$a_\gamma = 3.5467 + 0.467C_\gamma, \quad (2)$$

where  $a_\gamma$  is the lattice parameter of RA in  $\text{\AA}$ , and  $C_\gamma$  is the carbon content of RA in wt.%.

Rectangular tensile specimens with a gauge length of 50 mm and a width of 12.5 mm were cut along the rolling direction and tested using an Instron-8500 digital control tensile testing machine.

Tensile properties, content of RA, etc., were determined by the average values of tested results of five specimens, and the confidence intervals under the confidence level of 95 % were calculated.

### 3. Results and discussion

Figure 2 shows the metallographic microstructures of experimental steels subjected to different deformation processes. It can be seen that the volume fractions of microstructural constituents (polygonal ferrite and bainite) for the two processes are obviously different. For Process A, the microstructure contains more bainite but less polygonal ferrite, while opposite results are observed in the case of Process B.

It is difficult to discern RA under an optical microscope. Therefore, TEM analyses for RA were performed, and the results are shown in Figs. 3 and 4, respectively. In the case of Process A, as indicated in Fig. 3, RA particles are present in the form of thin interlayer films along bainitic ferrite lath boundaries. Moreover, from Fig. 3b, it is clearly visible

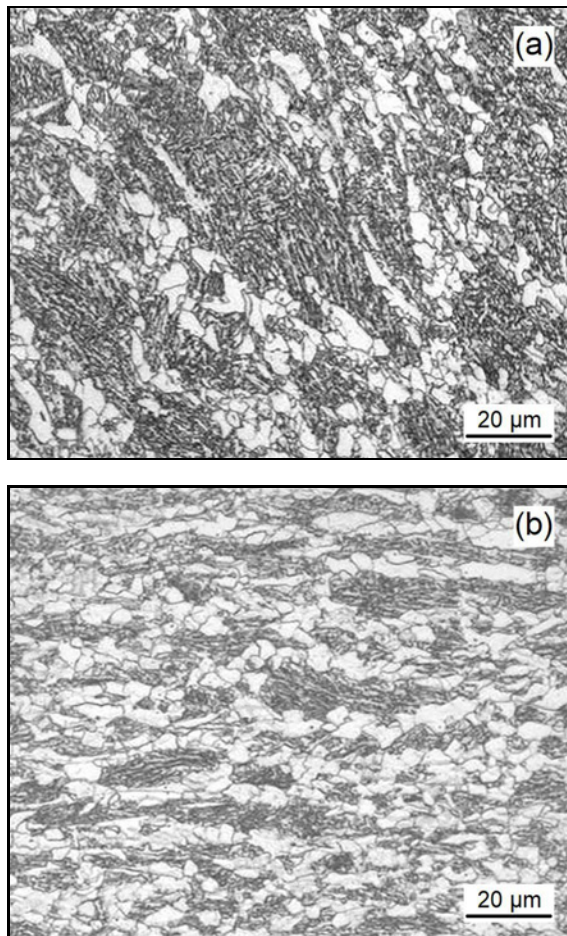


Fig. 2. Microstructures for experimental steels: (a) Process A, (b) Process B.

that RA has the Kurdjumov-Sachs (K-S) orientation relationship of  $\{011\}_{\text{Ferrite}}//\{111\}_{\text{Austenite}}$  and  $\langle 111 \rangle_{\text{Ferrite}}//\langle 011 \rangle_{\text{Austenite}}$  with adjacent bainitic ferrite.

Similar to Process A, in the microstructure for Process B steel, lamellar RA is also found to appear in the bainitic structure, and there exists definite orientation, i.e., Nishiyama-Wassermann (N-W) relationship of  $\{110\}_{\text{Ferrite}}//\{111\}_{\text{Austenite}}$  and  $\langle 100 \rangle_{\text{Ferrite}}//\langle 110 \rangle_{\text{Austenite}}$ , between RA and surrounding bainitic ferrite, as shown in Figs. 4a,b. However, compared to Process A, RA displays some differences from the view of morphology and distribution under the condition of Process B. Some blocky RA particles of different sizes are trapped in polygonal ferrite grains (Figs. 4c,d), and long RA strips and isolated RA islands are scattered in granular bainitic ferrite matrix (Figs. 4e,f).

In addition, the characteristics of bainite are a little different from those displayed in Process A. In the microstructure for Process B, as indicated in Fig. 4a, bainitic packets are usually separated and enclosed by polygonal ferrite and contain a small amount of

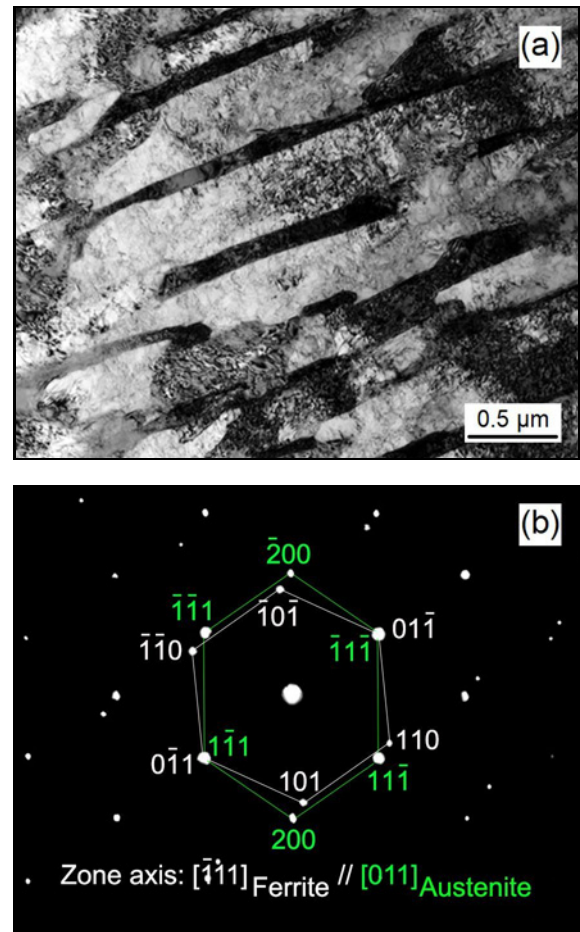


Fig. 3. TEM analyses of RA for Process A: (a) film-like RA distributed between bainite platelets, (b) selected area electron diffraction pattern (SADP) for RA.

bainitic ferrite platelets that have not developed well.

Figure 5 shows the XRD analysis results of RA under different processes. Based on the XRD patterns, the volume fractions of RA are calculated to be about 6.7% for Process A and about 11.0% for Process B, respectively. RA content for Process B is higher than that for Process A.

As shown above, the deformation process in the single-phase austenite region has a remarkable effect on the metallographic microstructures, especially RA characteristics. This is mainly due to the state change of prior austenite caused by deformation. It can be seen from Fig. 6 that deformation in the austenite non-recrystallization region can lead to austenite pancaking, i.e., strain-hardening state. The bigger reduction deformation results in a more remarkable pancaking phenomenon and, thus, a more significant strain-hardening effect in prior austenite.

In strain-hardened austenite, some crystal defects caused by accumulated strain in the non-recrystallization region, such as dislocation structure and deformed band, are formed [19–21]. Com-



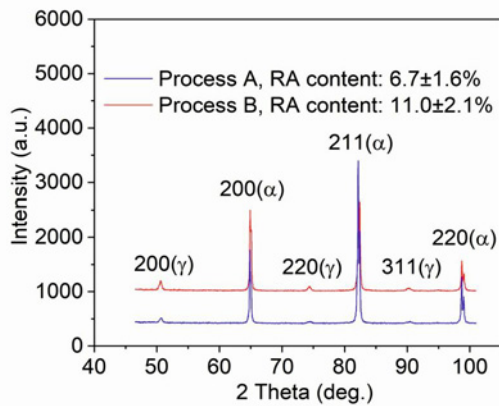


Fig. 5. XRD data of RA for different processes.

Moreover, forming a large amount of proeutectoid ferrite can cause noticeable carbon enrichment and decrease the remaining austenite surrounded by proeutectoid ferrite grains. For Process A, at the end of the intercritical region, the microstructure has opposite characteristics from the perspectives of the size, amount and carbon content of remaining austenite and the amount of proeutectoid ferrite.

During the holding at a temperature of 410°C, austenite to bainite transformation starts. As mentioned above, in the case of Process B, the remaining austenite has a small size and low volume fraction but contains a high density of dislocations and high average carbon content. Carbon enrichment in austenite decreases the driving force of bainitic transformation [26, 27], and tangled dislocations hinder the growth of bainitic ferrite by a displacive mechanism in austenite [28], which leads to chemical and mechanical stabilization of remaining austenite against bainite transformation. Moreover, the small size of remaining austenite prior to transformation limits the development of bainitic ferrite plates due to the impingement of a large amount of intragranular ferrite. As a result, the remaining austenite to bainite transformation does not develop fully, which, coupled with the factor of a small amount of remaining austenite, leads to a low bainite volume fraction in the room microstructure for Process B.

Generally, carbon enrichment is more remarkable in small austenite particles during the austenite-to-ferrite transformation [29, 30]. Moreover, small austenite particles have high mechanical stability against bainitic and martensitic transformations and, thus, contribute to the austenite retention [31]. In the case of Process B, among different-sized remaining austenite particles after the completion of the proeutectoid ferrite reaction, those with much smaller sizes could be stabilized during 410°C holding and subsequent air cooling and become blocky RA distributed

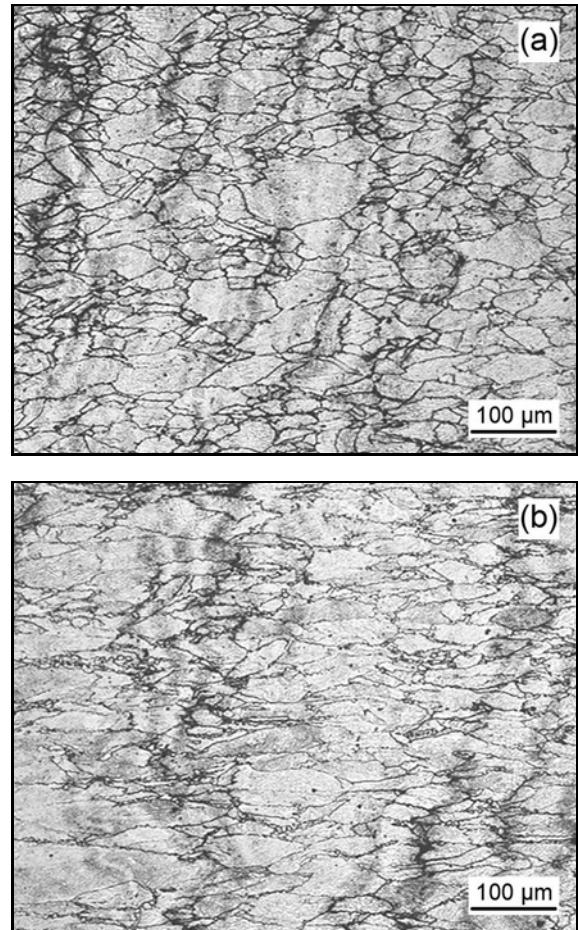


Fig. 6. Prior austenite morphology after different deformations: (a) Process A, (b) Process B.

in proeutectoid ferrite or at the grain boundaries of ferrite.

In contrast to Process B, austenite to bainite transformation develops extensively in the case of Process A because of less carbon enrichment and low density of crystal defect structures in remaining austenite. In addition, the large amount and particle size of remaining austenite are also factors causing a high-volume fraction of the transformation product of bainite in the microstructure. The formation of a large amount of bainite consumes dramatically remaining austenite accompanied by carbon enrichment in film-like residual austenite distributed between bainite platelets that can remain in room microstructure (i.e., RA). Consequently, although there is a high content of remaining austenite, the resulting volume fractions of RA are low.

The deformation processes in the non-recrystallization regions not only cause the aforementioned differences in microstructural characteristics but also have a strong influence on the mechanical properties of experimental steels. Therefore, the tensile prop-

Table 4. Mechanical properties of experimental steels

Processes	YS* (MPa)	UTS (MPa)	TEL (%)	UEL (%)	PSE (GPa·%)
A	541 ± 12	877 ± 24	22.9 ± 1.4	15.0 ± 1.1	20.1 ± 1.7
B	496 ± 16	814 ± 19	30.8 ± 2.4	22.1 ± 1.7	25.1 ± 1.7

\*The yield strength (YS) is defined as 0.2 % offset proof stress.

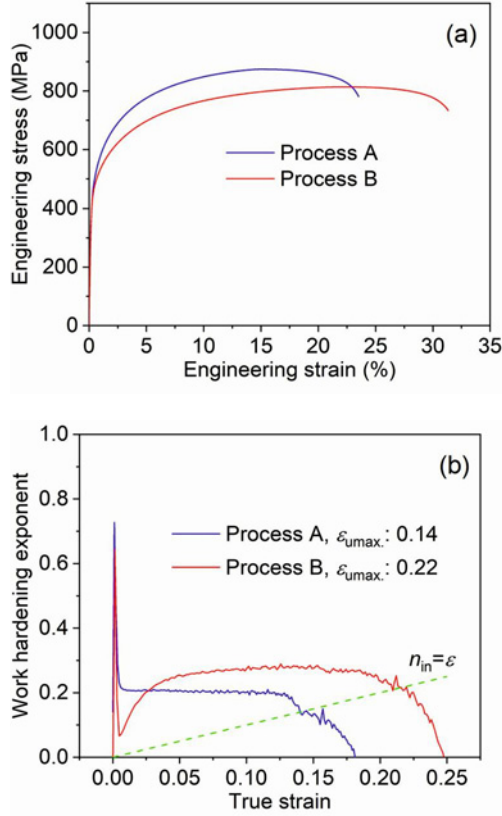


Fig. 7. Engineering stress-strain curves (a) and variation in instantaneous strain-hardening exponent versus true strain (b).

erties of experimental steels were tested, and representative tensile behavior curves are given in Fig. 7. From engineering stress-strain curves (Fig. 7a), yield strength (YS), ultimate tensile strength (UTS), total elongation (TEL) and the product of ultimate tensile strength and total elongation (PSE) are obtained and listed in Table 4. The engineering stress-strain ( $\sigma_e$ - $\epsilon_e$ ) curves obtained from the tensile tests were converted to true stress-strain ( $\sigma$ - $\epsilon$ ) ones using Eqs. (3) and (4) [1]:

$$\sigma = \sigma_e (1 + \epsilon_e), \quad (3)$$

$$\epsilon = \ln(1 + \epsilon_e). \quad (4)$$

Hollomon equation is usually used to describe the dependence of true stress and strain [32]. According

to the Hollomon equation (Eq. (5)), the instantaneous strain-hardening exponent ( $n_{in}$ ) is calculated using the following relationship [33], and  $n_{in}$  against  $\epsilon$  curves are drawn, as shown in Fig. 7b:

$$n_{in} = \frac{\epsilon}{\sigma} \frac{d\sigma}{d\epsilon}. \quad (5)$$

The instantaneous strain-hardening exponent  $n_{in}$  reflects the uniformly strained ability. When  $n_{in}$  is equal to  $\epsilon$ , necking is initiated [33]. Therefore, a designed  $n_{in} = \epsilon$  curve is also plotted in a green dot-dash line in Fig. 7b, and the points of intersection of the two kinds of curves indicate the values of maximum uniform true strain ( $\epsilon_{umax}$ ). Uniform elongation values (UEL) are calculated based on  $\epsilon_{umax}$  data using Eq. (4) and are listed in Table 4.

Tensile experimental results indicate that compared with Process A, the experimental steel for Process B exhibits a lower strength level but higher elongation (including total elongation and uniform elongation) and is the product of ultimate tensile strength and total elongation. This is attributed to the differences in RA characteristics along with the volume fraction of microstructural constituents in the microstructures for the two processes. For Process B, the TRIP effect of a large amount of different-sized RA particles remarkably improves the ductility during tensile deformation. Besides, the higher proportion of polygonal ferrite (correspondingly, lower bainite amount) also enhances elongation to some extent but decreases strength.

The contribution of the TRIP effect for RA to the ductility can be analyzed well from the strain-hardening behavior shown in Fig. 7b. In the initial stage of deformation,  $n_{in}$  values for two experimental steels all decrease quickly to minimum level because of dynamic restoration of soft strained ferrite [34, 35]. For Process A steel, the minimum  $n_{in}$  value is higher than that for Process B steel because of a larger amount of bainite with a high density of dislocations. After that, two experimental steels show different strain dependence with an increase in strain. In Process B steel,  $n_{in}$  value is gradually increased with strain and maintained at a higher level over a considerably wide strain range before the onset of necking. On the contrary, for Process A steel, the  $n_{in}$  value remains lower and nearly constant over a narrower strain scope without increasing in  $n_{in}$  value over the entire strain range.

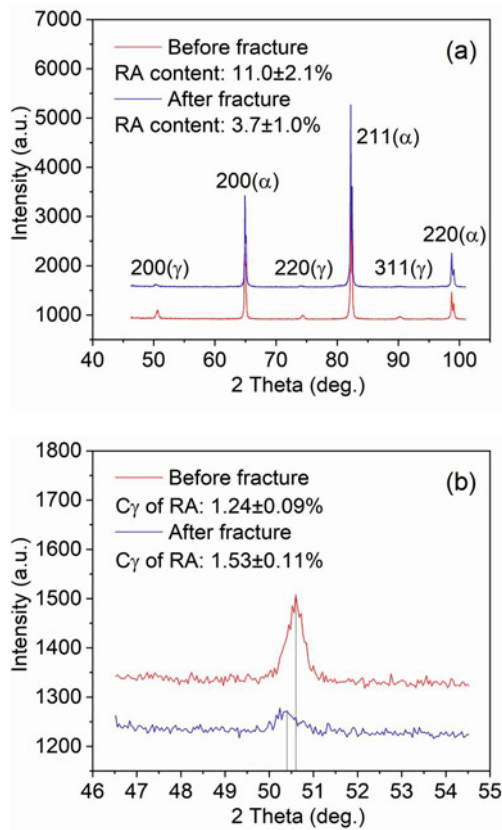


Fig. 8. XRD patterns for Process B steel used to calculate (a) RA content and (b) average carbon content in RA before and after tensile fracture.

As mentioned above, small-sized RA particles have high stability against deformation induced transformation to martensite due to higher carbon enrichment and size effect. Moreover, the kind of neighboring phase around RA also plays an important role in RA stability [36, 37]. Soft polygonal ferrite matrix around RA can absorb the volume expansion resulting from martensite transformation and is disadvantageous to RA retention during strain. Conversely, bainitic ferrite can act as a shield for enclosed RA and effectively prevent stress or strain from imposing on RA due to higher yield strength, suppressing the austenite to martensite transformation during deformation. Therefore, film-like RA existing along bainite lath boundary or long strip RA lying in granular bainitic ferrite possess higher stability than those embedded in polygonal ferrite or presented at ferrite boundary under the same carbon content and particle size.

For Process B steel, a large amount of big blocky RA with low stability easily transforms to martensite in the early stage of deformation and results in a significant strain-hardening effect, causing a fast and marked increase in  $n_{in}$  value. With increased strain, smaller-sized blocky RA and lamellar along with long strip RA begin to gradually and continually trans-

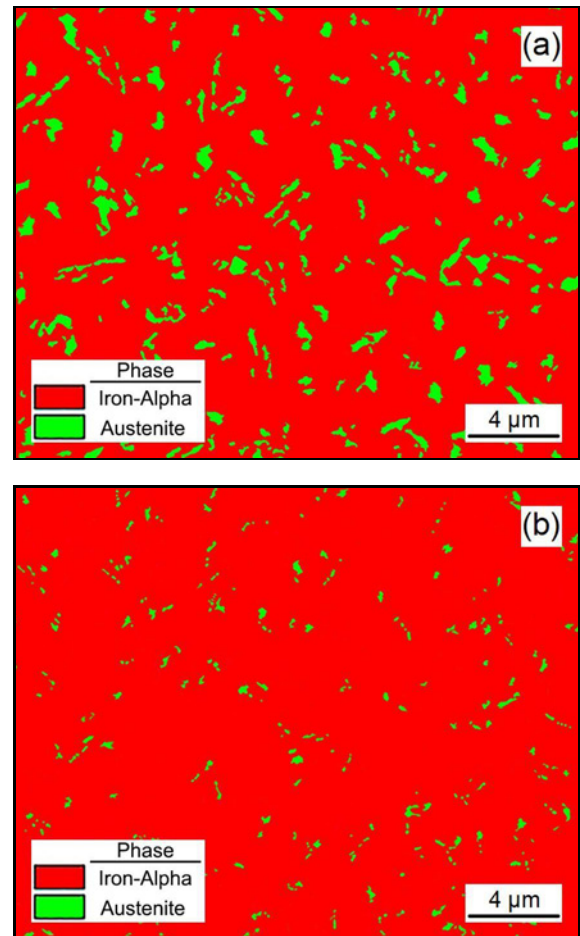


Fig. 9. EBSD phase maps of Process B steel before (a) and after (b) tensile fracture.

form to martensite owing to higher stability, keeping a higher  $n_{in}$  value over a wide strain region. This gradual and sustained strain-hardening effect can effectively inhibit the necking initiation and extend uniform deformation to a high strain level, which produces a noticeable TRIP effect and thus dramatically improves the ductility. During further straining, due to the consumption of a large amount of RA (as shown in subsequent Fig. 8), the strain-hardening effect gets weakened, accompanied by the occurrence of necking.

For Process A steel without different-sized blocky RA, a small amount of film-like RA in the bainitic structure provides a weak and transient TRIP effect, resulting in lower elongation and a poorer combination of ductility and strength compared with Process B steel.

Figure 8 shows the XRD data of RA before and after tensile fracture. It can be seen from Fig. 8a that after fracture, RA diffraction peaks have notably low intensities. The calculation results show that the content of RA after fracture is decreased strikingly from about 11.0 to 3.7% or so, indicating that a large amount of

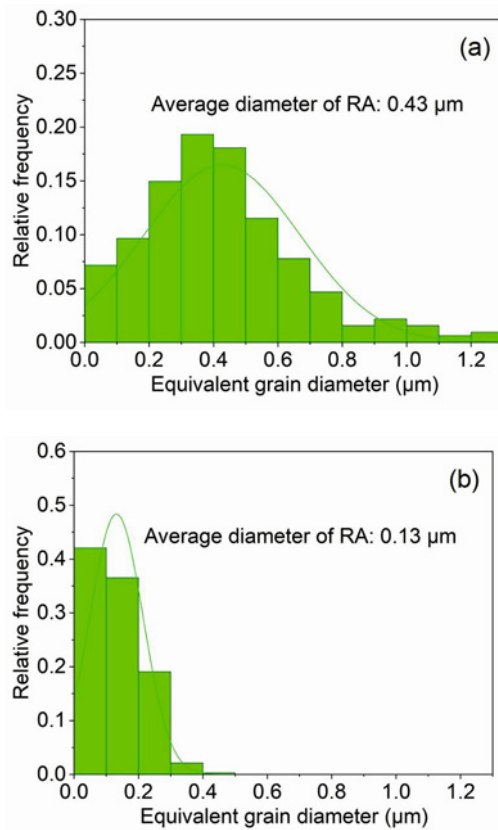


Fig. 10. Distribution for particle size of RA in Process B steel before (a) and after (b) tensile fracture.

RA transforms to martensite during tensile deformation. Moreover, carbon content is calculated based on  $(200)_{\gamma}$  diffraction peaks of RA in Fig. 8b, which illustrates that un-transformed RA after fracture has higher carbon concentration compared with that before fracture.

Figure 9 indicates EBSD results for RA before and after tensile fracture, which intuitively demonstrates RA particle size change before and after tensile fracture. It is obvious that after fracture, the particle size of un-transformed RA becomes much smaller in comparison to that before fracture. Statistics results on RA particle size are shown in Fig. 10. Before fracture, the particle diameter of RA varies continually from small to big and mainly distributes between 0.2 and 0.6 μm. The RA particle's average diameter is about 0.43 μm. After a fracture, RA particles with a diameter of more than 0.4 μm almost disappear, and particles less than 0.2 μm in diameter have a very high-count frequency. The average diameter of RA particles is decreased to 0.13 μm. The above results reveal again that RA, with a small size and high carbon content, has high stability.

#### 4. Conclusions

(1) The bigger reduction in austenite non-recrystallization region results in more notable pancaking of austenite grain. This austenite condition strongly promotes the proeutectoid ferrite formation, which causes an increase in the amount of RA.

(2) Compared with the case of smaller reduction in austenite non-recrystallization region, the steel with bigger reduction exhibits higher elongation and excellent combination of strength and ductility because of higher fractions of polygonal ferrite and RA particles with different sizes that provide sustained TRIP effect over a significantly wide strain range.

(3) The un-transformed RA in fractured tensile specimen has a much smaller grain size and higher carbon content in comparison to the case before fracture.

#### Acknowledgements

This work was financially supported by a Project of the Education Department of Liaoning Province (Grant no. LJKMZ20220743). The authors are grateful to Drs. H. Y. Wu and J. F. Wang (State Key Laboratory of Rolling & Automation of Northeastern University, P. R. China) for providing help in TEM and EBSD analyses works.

#### References

- [1] A. Grajcar, A. Skowronek, K. Radwanski, Mechanical behavior and stability of dispersed retained austenite in thermomechanically rolled and isothermally-treated TRIP-aided multiphase steel, *Mater. Sci. Eng. A* 830 (2022) 142300. <https://doi.org/10.1016/j.msea.2021.142300>
- [2] I. B. Timokhina, P. D. Hodgson, E. V. Pereloma, Effect of deformation schedule on the microstructure and mechanical properties of a thermomechanically processed C-Mn-Si transformation-induced plasticity steel, *Metall. Mater. Trans. A* 34 (2003) 1599–1609. <https://doi.org/10.1007/s11661-003-0305-8>
- [3] R. Ranjan, H. Beladi, P. D. Hodgson, S. B. Singh, The mechanical properties of low alloy TRIP-aided steel: The role of retained austenite, *Metall. Mater. Trans. A* 52 (2021) 4649–4663. <https://doi.org/10.1007/s11661-021-06417-z>
- [4] M. Soleimani, A. Kalhor, H. Mirzadeh, Transformation-induced plasticity (TRIP) in advanced steels: A review, *Mater. Sci. Eng. A* 795 (2020) 140023. <https://doi.org/10.1016/j.msea.2020.140023>
- [5] V. L. Nuam, H. Zhang, Y. C. Wang, Z. P. Xiong, Role of retained austenite in advanced high-strength steel: Ductility and toughness, *J. Iron Steel Res. Int.* 31 (2024) 2079–2089. <https://doi.org/10.1007/s42243-023-01165-3>
- [6] W. Q. Mao, S. Gao, W. Gong, Y. Bai, S. Harjo, M.-H. Park, A. Shibata, N. Tsuji, Quantitatively evaluating the respective contribution of austenite and

- deformation-induced martensite to flow stress, plastic strain, and strain hardening rate in tensile deformed TRIP steel, *Acta Mater.* 256 (2023) 119139. <https://doi.org/10.1016/j.actamat.2023.119139>
- [7] N. Tsuchida, Preface to the special issue on “Advances in TRIP effect research”, *ISIJ Int.* 61 (2021) 517. <https://doi.org/10.2355/isijinternational.61.517>
- [8] J. Peng, L. Shi, L. F. Li, C. J. Huang, W. T. Sun, Y. I. Huang, J. J. Dai, R. Bao, B. T. Zhang, Stability of retained austenite and its effect on tensile properties and hole expansion performance of high-strength steel, *Mater. Sci. Eng. A* 914 (2024) 147112. <https://doi.org/10.1016/j.msea.2024.147112>
- [9] D. M. Xu, D. K. Zhang, G. W. Yang, Q. Wang, S. Q. Bao, G. Zhao, Effect of quenching temperature on the austenite stability and mechanical properties of high-strength air-cooled TRIP steel prepared with hot-rolled C–Si–Mn sheets, *J. Mater. Res. Technol.* 31 (2024) 420–433. <https://doi.org/10.1016/j.jmrt.2024.06.044>
- [10] H. X. Zuo, J. F. Feng, Y. Sun, Q. N. Li, Z. C. Li, D. Misra, L. F. He, H. P. Li, Microstructure-mechanical property relationship and austenite stability in transformation-induced plasticity steels: Effects of quenching and partitioning processing and quenching and tempering treatments, *J. Mater. Eng. Perform.* 33 (2024) 3384–3396. <https://doi.org/10.1007/s11665-023-08240-6>
- [11] H. Nasr El-Din, R. Reda, Retained austenite attributes and mechanical performance of different compositions of TRIP steel alloys, *J. Mater. Eng. Perform.* 28 (2019) 2167–2177. <https://doi.org/10.1007/s11665-019-04010-5>
- [12] J. N. Huang, Z. Y. Tang, H. Ding, R. D. K. Misra, The significant impact of phase fraction and austenite stability on the mechanical properties of a low-alloyed TRIP-aided steel: An insight into experimental analysis and predictions, *Mater. Sci. Eng. A* 759 (2019) 40–46. <https://doi.org/10.1016/j.msea.2019.05.026>
- [13] M. Gomez, C. I. Garcia, A. J. Deardo, The role of new ferrite on retained austenite stabilization in Al-TRIP steels, *ISIJ Int.* 50 (2010) 139–146. <https://doi.org/10.2355/isijinternational.50.139>
- [14] Y. Onuki, T. Hirano, A. Hoshikawa, S. Sato, T. Tomida, In situ observation of bainite transformation and simultaneous carbon enrichment in austenite in low-alloyed TRIP steel using time-of-flight neutron diffraction techniques, *Metall. Mater. Trans. A* 50 (2019) 4977–4986. <https://doi.org/10.1007/s11661-019-05415-6>
- [15] S. C. Chen, Y. T. Wang, Y. C. Lin, C. Y. Huang, J. R. Yang, H. W. Yen, Microstructure and mechanical behaviors of GPa-grade TRIP steels enabled by hot-rolling processes, *Mater. Sci. Eng. A* 761 (2019) 138005. <https://doi.org/10.1016/j.msea.2019.06.015>
- [16] X. H. Wang, J. Kang, Y. J. Li, G. Yuan, R. D. K. Misra, G. D. Wang, Effect of deformation parameters in unrecrystallization range on microstructural characteristics in Al-bearing hot-rolled TRIP steel, *J. Iron Steel Res. Int.* 26 (2019) 1329–1339. <https://doi.org/10.1007/s42243-019-00327-6>
- [17] F. Alharbi, A. A. Gazder, A. Kostryzhev, B. C. De Cooman, E. V. Pereloma, The effect of processing parameters on the microstructure and mechanical properties of low-Si transformation-induced plasticity steels, *J. Mater. Sci.* 49 (2014) 2960–2974. <https://doi.org/10.1007/s10853-013-8008-z>
- [18] B. Zhang, L. X. Du, Y. Dong, D. X. Han, H. Y. Wu, F. H. Lu, R. D. K. Misra, Structure-property relationship in novel low carbon hot-rolled TRIP steels via thermo-mechanical controlled processing and coiling, *Mater. Sci. Eng. A* 771 (2020) 138643. <https://doi.org/10.1016/j.msea.2019.138643>
- [19] S. M. K. Hosseini, A. Zaeri-Hanzaki, S. Yue, Effect of austenite deformation in the non-recrystallization region on microstructure development in low-silicon content TRIP-assisted steels, *Mater. Sci. Eng. A* 618 (2014) 63–70. <https://doi.org/10.1016/j.msea.2014.08.059>
- [20] Q. X. Feng, L. F. Li, W. Y. Yang, Z. Q. Sun, Microstructures and mechanical properties of hot-rolled Nb-microalloyed TRIP steels by different thermo-mechanical processes, *Mater. Sci. Eng. A* 605 (2014) 14–21. <https://doi.org/10.1016/j.msea.2014.03.051>
- [21] L. Y. Lan, W. Zhou, R. D. K. Misra, Effect of hot deformation parameters on flow stress and microstructure in a low carbon microalloyed steel, *Mater. Sci. Eng. A* 756 (2019) 18–26. <https://doi.org/10.1016/j.msea.2019.04.039>
- [22] A. Grajcar, P. Skrzypczyk, R. Kuziak, K. Gołombek, Effect of finishing hot-working temperature on microstructure of thermomechanically processed Mn-Al multiphase steels, *Steel Res. Int.* 85 (2014) 1058–1069. <https://doi.org/10.1002/srin.201300227>
- [23] L. Liu, B. B. He, G. J. Cheng, H. W. Yen, M. X. Huang, Optimum properties of quenching and partitioning steels achieved by balancing fraction and stability of retained austenite, *Scr. Mater.* 150 (2018) 1–6. <https://doi.org/10.1016/j.scriptamat.2018.02.035>
- [24] X. X. Dong, S. Liu, Y. F. Shen, N. Jia, Isothermal holding treatment of a transformation-induced plasticity steel for obtaining ultrahigh strength and high plasticity, *J. Mater. Eng. Perform.* 30 (2021) 4504–4517. <https://doi.org/10.1007/s11665-021-05728-x>
- [25] X. L. Li, Y. J. Li, J. Kang, C. N. Li, G. Yuan, G. D. Wang, Control of carbon content in steel by introducing proeutectoid ferrite transformation into hot-rolled Q&P process, *J. Mater. Eng. Perform.* 27 (2018) 315–323. <https://doi.org/10.1007/s11665-017-3093-9>
- [26] R. Ranjan, H. Beladi, S. B. Singh, P. D. Hodgson, Thermo-mechanical processing of TRIP-aided steels, *Metall. Mater. Trans. A* 46 (2015) 3232–3247. <https://doi.org/10.1007/s11661-015-2885-5>
- [27] T. Nakagaito, H. Matsuda, Y. Nagataki, K. Seto, Effects of partitioning of manganese and silicon during intercritical annealing on transformation behavior and mechanical properties of low alloyed TRIP-assisted steel sheets, *ISIJ Int.* 57 (2017) 380–387. <http://dx.doi.org/10.2355/isijinternational.ISIJINT-2016-288>
- [28] S. Lin, A. Borgenstam, A. Stark, P. Hedström, Effect of Si on bainitic transformation kinetics in steels explained by carbon partitioning, carbide formation, dislocation densities, and thermodynamic conditions, *Mater. Charact.* 185 (2022) 111774. <https://doi.org/10.1016/j.matchar.2022.111774>

- [29] H. S. Park, J. C. Han, N. S. Lim, J.-B. Seo, C. G. Park, Nano-scale observation on the transformation behavior and mechanical stability of individual retained austenite in CMnSiAl TRIP steels, *Mater. Sci. Eng. A* 627 (2015) 262–269. <https://doi.org/10.1016/j.msea.2015.01.005>
- [30] G. Liu, S. G. Zhang, J. Li, J. Wang, Q. G. Meng, Fast-heating for intercritical annealing of cold-rolled quenching and partitioning steel, *Mater. Sci. Eng. A* 669 (2016) 387–395. <https://doi.org/10.1016/j.msea.2016.05.106>
- [31] T. Hanamura, S. Torizuka, S. Tamura, S. Enokida, H. Takechi, Effect of austenite grain size on transformation behavior, microstructure and mechanical properties of 0.1C-5Mn martensitic steel, *ISIJ Int.* 53 (2013) 2218–2225. <http://dx.doi.org/10.2355/isijinternational.53.2218>
- [32] A. Karimi, S. Kheirandish, M. Mahmoudiniya, Effect of bainite volume fraction on mechanical properties of a ferrite-bainite-martensite steel, *Kovove Mater.* 55 (2017) 175–182. [https://doi.org/10.4149/km\\_2017\\_3\\_175](https://doi.org/10.4149/km_2017_3_175)
- [33] H. Kong, Q. Chao, M. H. Cai, E. J. Pavlina, B. Rolfe, P. D. Hodgson, H. Beladi, Microstructure evolution and mechanical behavior of a CMn-SiAl TRIP steel subjected to partial austenitization along with quenching and partitioning treatment, *Metall. Mater. Trans. A* 49 (2018) 1509–1519. <https://doi.org/10.1007/s11661-018-4525-3>
- [34] D. Q. Zou, S. H. Li, J. He, Temperature and strain rate dependent deformation induced martensitic transformation and flow behavior of quenching and partitioning steels, *Mater. Sci. Eng. A* 680 (2017) 54–63. <https://doi.org/10.1016/j.msea.2016.10.083>
- [35] H. Rastegari, A. Kermanpur, A. Najafizadeh, Effect of initial microstructure on the work hardening behavior of plain eutectoid steel, *Mater. Sci. Eng. A* 632 (2015) 103–109. <https://doi.org/10.1016/j.msea.2015.02.040>
- [36] A. Lavakumar, M.-H. Park, S. Hwang, H. Adachi, M. Sato, R. K. Ray, M. Murayama, N. Tsuji, Role of surrounding phases on deformation-induced martensitic transformation of retained austenite in multi-phase TRIP steel, *Mater. Sci. Eng. A* 874 (2023) 145089. <https://doi.org/10.1016/j.msea.2023.145089>
- [37] X. D. Tan, H. S. He, W. J. Lu, L. Yang, B. Tang, J. Yan, Y. B. Xu, D. Wu, Effect of matrix structures on TRIP effect and mechanical properties of low-C low-Si Al-added hot-rolled TRIP steels, *Mater. Sci. Eng. A* 771 (2020) 138629. <https://doi.org/10.1016/j.msea.2019.138629>